Symmetry or asymmetry: which is the altar of nitrogen vacancies for alkaline hydrogen evolution

Yu Zhang, Yingxin Ma, Wenfang Yuan, Lejuan Cai,* Yang Chai, Bocheng Qiu*

Experimental Section

Preparation of Cr-Co₄N-Nᵥ/NF: One piece of Ni foam (NF, 2*5 cm) was washed by diluted hydrochloric acid, acetone, and deionized water (DI water) in turn, and eventually dried using nitrogen flow. The washed NF was immersed in a mixed solution containing 1 mmol cobalt nitrate, 0.1 mmol chromium nitrate, 4 mmol ammonium fluoride, and 5 mmol urea, which was then transferred into 50 mL stainless-steel autoclave and kept at 120 °C for 10 h. The Cr-Co(OH)F/NF was washed using DI water and dried at 40 °C for overnight. The Cr-Co₄N/NF with the measured mole ratio of Cr/Co (1:10.3) was obtained via the thermal treatment with Cr-Co(OH)F/NF under NH_3 atmosphere at 480 °C, and the loading density of Cr-Co₄N across the entire NF substrate was determined to be approximately 0.80 mg cm⁻². As a control, we prepared Cr-Co₄N/NF with other Cr/Co mole ratioes (1:19.2 and 1:4.8) via controling the addition amount of Cr precursor at 0.05 and 0.2 mmol, respectively. For clairty, the Cr-Co₄N/NF mentioned in this Article refers to the catalyst with the optimal Cr doping level (Cr:Co=1:10.3), unless otherwise stated. The Cr-Co₄N-Nᵥ/NF with the loading density of 0.70 mg cm⁻² was synthesized by annealing the prepared Cr-Co₄N/NF at 400 °C under H_2/N_2 atmosphere for 30 min. The preparation method of Co₄N-Nᵥ/NF is similar to that of Cr-Co₄N-Nᵥ/NF, except that chromium nitrate is absent. The loading densities of all the prepared catalysts on the NF substrate were controlled at about 0.60 mg cm⁻² via ultrasonic treatment.

Characterizations

Scanning electron microscope (SEM; Hitachi S4800), transmission electron microscope (TEM; JEOL2011), and high resolution transmission electron microscope (HRTEM; JEOL 2100F) were utilized to observe the morphologies of the as-prepared catalysts. The element composition was analyzed by energy-dispersive X-ray spectroscopy (EDX) attached to the JEOL 2100F. X-ray photoelectron spectroscopy (XPS, Perkin-Elmer PHI 5000C ESCA system) was collected under Al Kα radiation operated at 250 W. Soft X-ray absorption spectroscopy (sXAS) spectra were carried out at beamline station BL12B in National Synchrotron Radiation Laboratory (NSRL), China, operated at 800 MeV with a maximum current of 300 mA. Ultraviolet photoelectron spectroscopy was performed on Thermo Scientific™ K-Alpha using He I resonance lines (hv = 21.22 eV), and the work function (Φ) is calculated by using the following equation: $\Phi = hv + E_{cutoff} - E_F$ (E_{cutoff} indicates the secondary electron cutoff energy and is obtained from the intersection of tangential lines drawn on the high-binding-energy cutoff of the UPS spectrum with the zero intensity line, while E_F refers to the Fermi level and is taken as 0). To confirm the crystal structure, X-ray diffraction (XRD) patterns of all the samples were collected in the range from 10° to 80° (2θ) using a Rigaku D/MAX IIIA 2550 diffract meter (Cu Kα radiation, λ = 1.5406 Å) operated at 40 kV and 100 mA. *In-situ* Raman spectra were recorded on a confocal Raman spectrometer (WITec alpha300 R) using an excitation wavelength of 532 nm and a laser power of 3 mW, and the chronoamperometry measurements were carried out by applying the desired potential ranging from open circuit potential (OCP) to -0.2 V vs. RHE in a 30 mL electrolyte (1 M KOH). Cr doping concentrations on the as-prepared

catalysts were determined by inductively coupled plasma mass spectrometry (ICP-MS, Shimadzu ICPS-7500 spectrometer).

Electrochemical measurements

To evaulate the HER activity fairly, the loading densities of all the prepared catalysts on the NF substrate (0.5*0.5 cm) were controlled at 0.60 mg cm^{-2} via ultrasonic treatment. The Pt/C supported by NF was prepared with the same loading density of 0.60 mg cm^{-2} (Note that the Pt loading density was calculated to be 0.12 mg cm^{-2}). Graphite and Hg/HgO electrode were used as the counter electrode and reference electrode, respectively. Potentials were referenced to a reversible hydrogen electrode (RHE): $E_{RHE}=E_{Hg/HgO} + 0.924$. The thermodynamic potential of Hg/HgO for HER in 1 M KOH was calibrated using the previous method,[1] which was determined to be -0.924 V. The overpotential (η) was calculated according to the following formula: $\eta= E_{RHE}$. Linear sweep voltammetry (LSV) was recorded in a H$_2$-saturated 1.0 M KOH at a scan rate of 5 mV s^{-1}. All the LSV curves presented in this Article were corrected for IR loss (The introduction of IR corrected polarization curves makes up for the electrode potential loss induced by the solution resistance). The durability measurements were carried out using cyclic voltammetry (CV) sweeps from -0.2 to 0.1 V (*vs.* RHE) at the scan rate of 50 mV s^{-1} for 2000 cycles and chronopotentiometry at a constant current density of 50 mA cm^{-2}. The electrochemical impendence spectroscopy (EIS) measurements were measured at an overpotential of 100 mV in the frequency range from 0.1 to 100 kHz with an amplitude of 5 mV. The electrochemical active surface area (ECSA) was calculated from the CV curves measured in a potential range from 0.15 to 0.25 V (E *vs.* RHE) in terms of the following equation: $C_{dl} = (j_a - j_c)/(2•v) = \Delta j/(2•v)$, where C_{dl}, j_a, j_c and v are the double-layer capacitance (F cm^{-2}), the anodic current density (mA cm^{-2}), the cathodic current density (mA cm^{-2}), and scan rate (mV s^{-1}), respectively. Note that j_a and j_c were recorded at 0.20 V (*vs.* RHE) and the slope of the Δj *vs* scan rate curve is just twice of the value of C_{dl}. The roughness factors (RF) of different samples from their C_{dl} values by using the equation: $RF = C_{dl}/C_s$, where C_s is the double layer capacitance of an ideally flat electrode, which is usually taken as 40 μF cm^{-2} in an alkaline electrolyte according to the typical references.[2] The turnover frequency (TOF) was calculated by the following equation: TOF= I/2Fn, where I, F, and n refer to the current during the linear CV sweep, the Faraday constant, and the number of active sites, respectively. The number of the active sites (n) was measured by CV scanning recorded from -0.2 to 0.6 V *vs.* RHE under neutral conditions at a scan rate of 50 mV s^{-1} and subsequently calculated by the following equation: n = Q/2F (Q means the whole charge of CV curve).

Theoretical simulations

The Vienna Ab initio Simulation Package was utilized to conduct density functional calculations, employing the Perdew, Burke and Ernzerhof (PBE) functional to describe exchange-correlation interactions and the projector augmented-wave method to represent core-valence electron interactions.[3, 4] The energy cutoff was set to 520 eV, and the convergence criteria for energy and force were established at below 10^{-5}

eV/atom and 0.01 eV Å^{-1}, respectively. Firstly, a (2×2) Co_4N (100) slab was optimized with six atomic layers. Then, the pristine Co_4N (100), Co_4N (100) with Cr dopant, Co_4N (100) with N vacancy, and Co_4N (100) with Cr dopant and N vacancy, are all considered. The adsorption energies of H_2O and H* on these substrates were calculated using the formula of $G_{ads} = G_{H2O/H*+sub} - (G_{H2O/H*} + E_{sub})$, where $G_{H2O/H*+sub}$ is the Gibbs energy of the substrate with adsorbed H_2O/H*, $G_{H2O/H*}$ is the Gibbs energy of the H_2O or H* adsorbate, and E_{sub} is the energy of the substrate. The Gibbs energy was estimated by accounting for the zero-point energy and Entropy corrections under the standard conditions (p_0 = 1 bar and T_0 = 298.15 K).[5] The chemical potential of proton and electron was described based on the computational hydrogen electrode.[6] The vdw-DF2 method was used to describe the van der Waals interactions for a better description of the interactions between the adsorbates and substrates.[7, 8] To avoid spurious interaction between adjacent slabs, the vacuum layer was set as 20 Å. The Brillouin zone was sampled using Monkhorst–Pack meshes of $4 \times 4 \times 1$ in all the adsorption calculations.
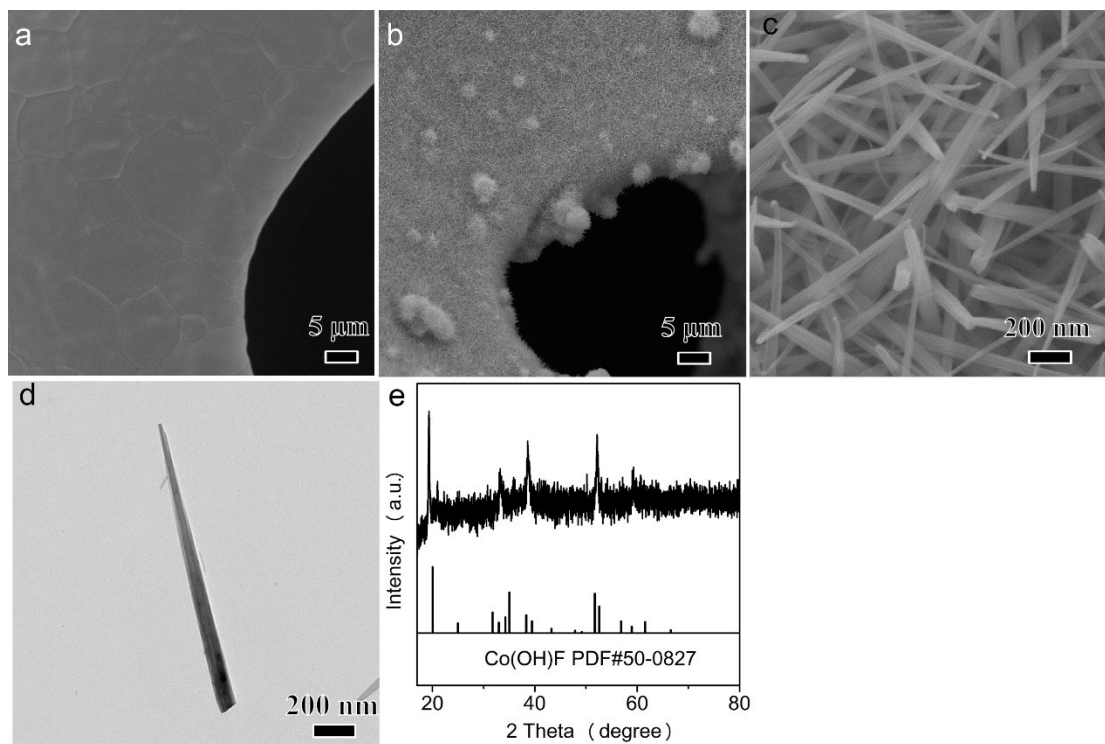
Fig. S1 (a) SEM image of pristine NF. (b,c) SEM and (d) TEM images of Cr-Co(OH)F/NF. (e) XRD pattern of Cr-Co(OH)F powder scraped from Cr-Co(OH)F/NF.
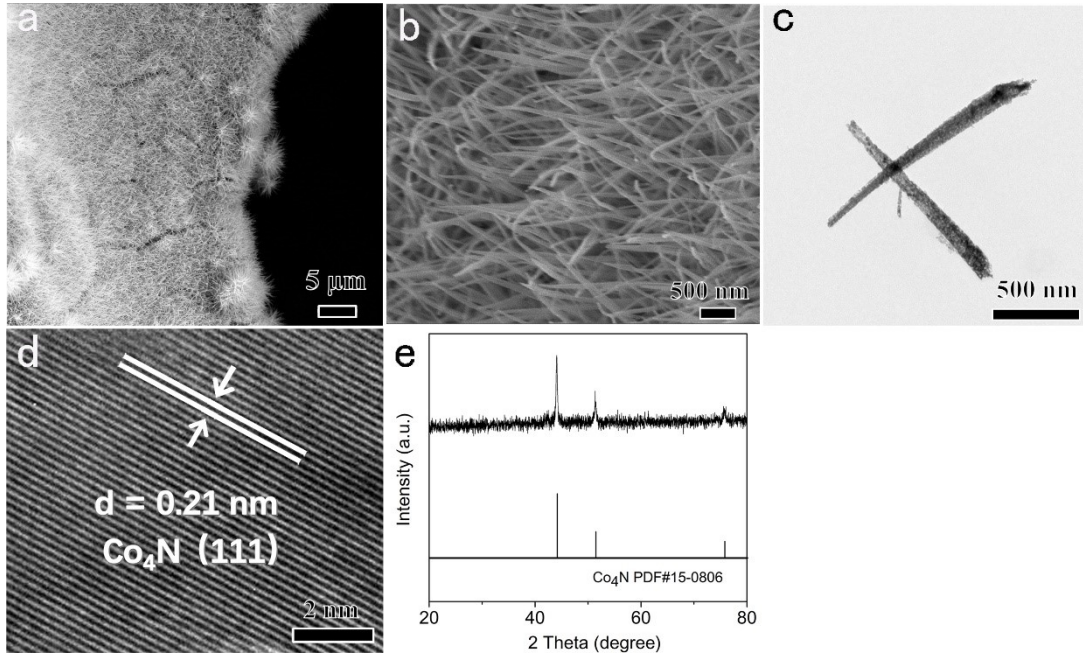
Fig. S2 (a,b) SEM images, (c) TEM image, and (d) HRTEM image of the as-prepared Cr-Co$_4$N/NF. (e) XRD pattern of Cr-Co$_4$N powders scraped from NF substrate.
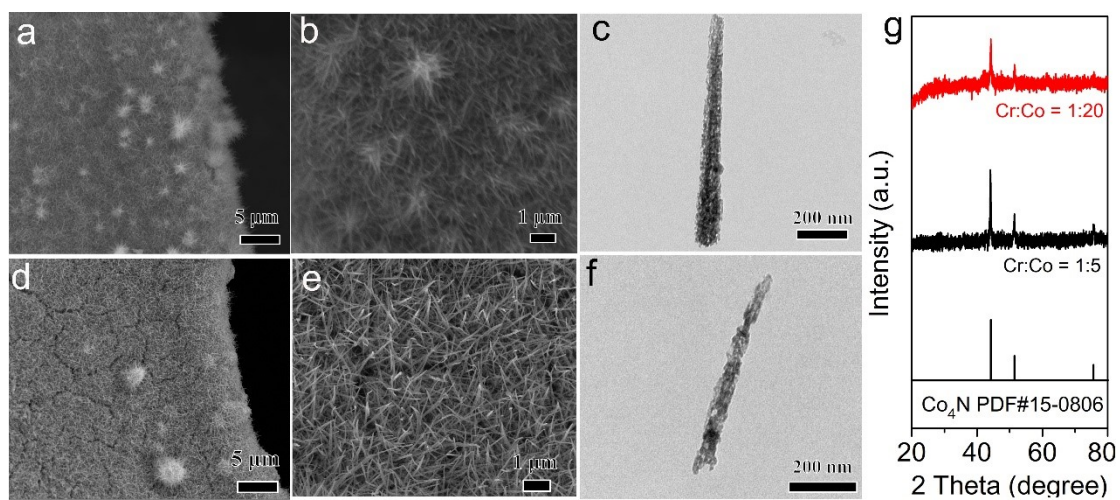
Fig. S3 SEM and TEM images of the as-prepared Cr-Co$_4$N/NF with different Cr/Co molar ratios: (a-c) Cr:Co = 1:20 and (d-f) Cr:Co = 1:5. (g) XRD patterns of the as-prepared Cr-Co$_4$N with different Cr/Co mole ratios scraped from NF substrate.
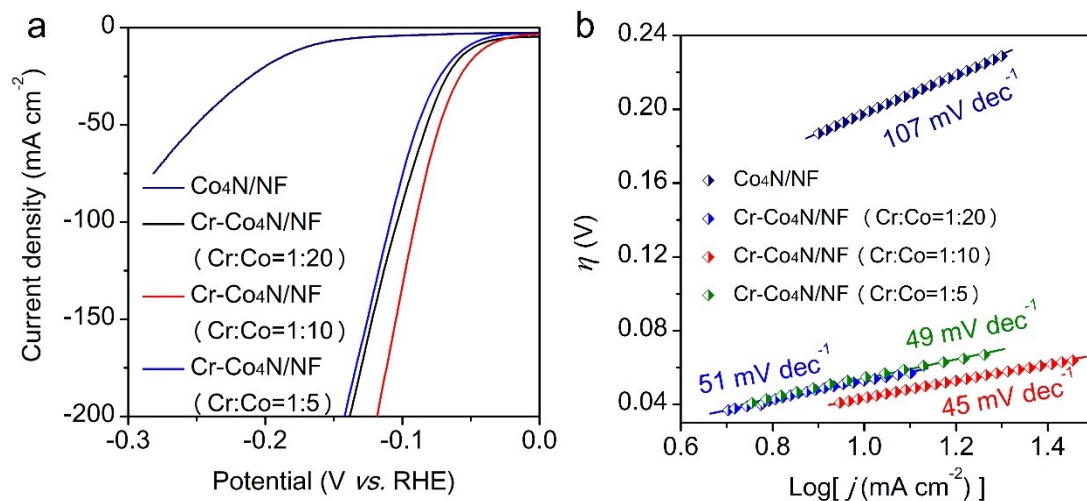
Fig. S4 The optimal Cr doping concentration investigations confirmed by HER measurements: (a) LSV curves and (b) Tafel slopes.
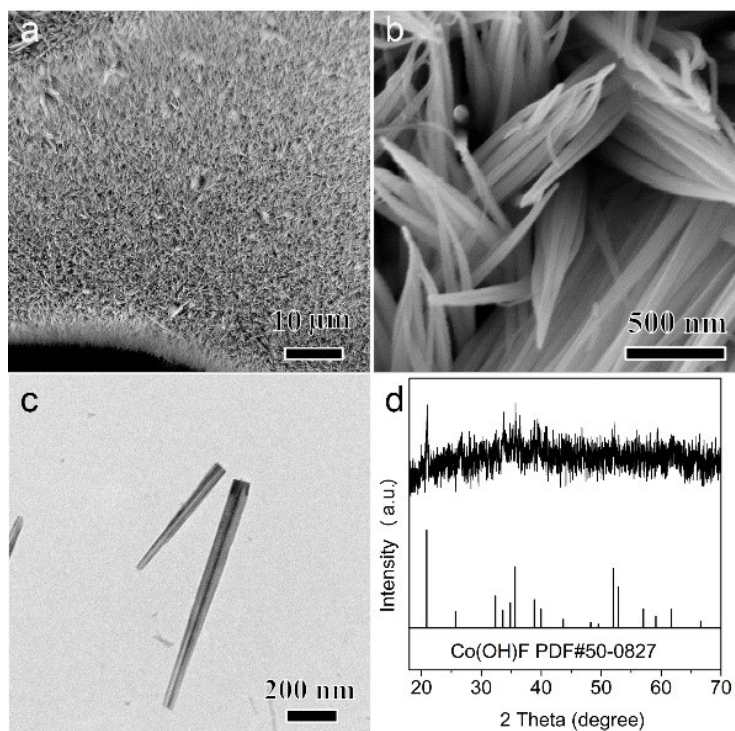
Fig. S5 (a,b) SEM and (c) TEM images of the as-prepared Co(OH)F/NF. (d) XRD pattern of Co(OH)F powder scraped from NF substrate.
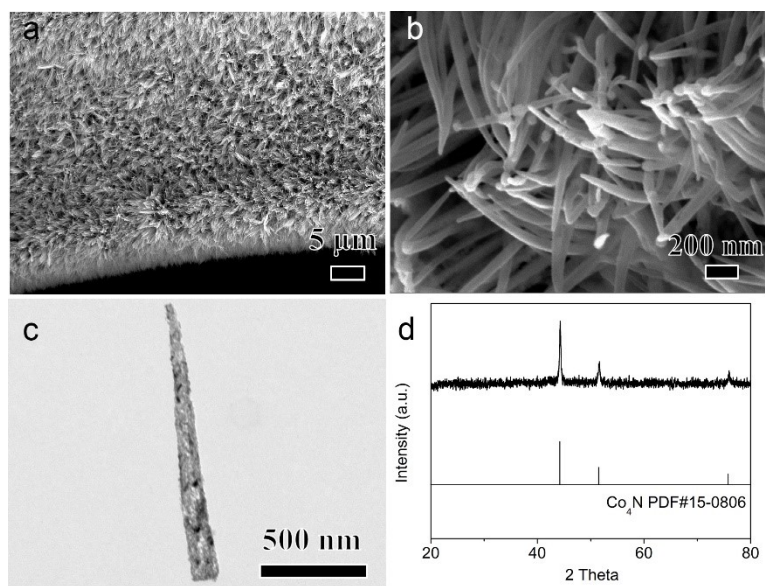
Fig. S6 (a,b) SEM and (c) TEM images of the as-prepared Co_4N/NF. (d) The XRD pattern of Co_4N powder scraped from NF substrate.

.
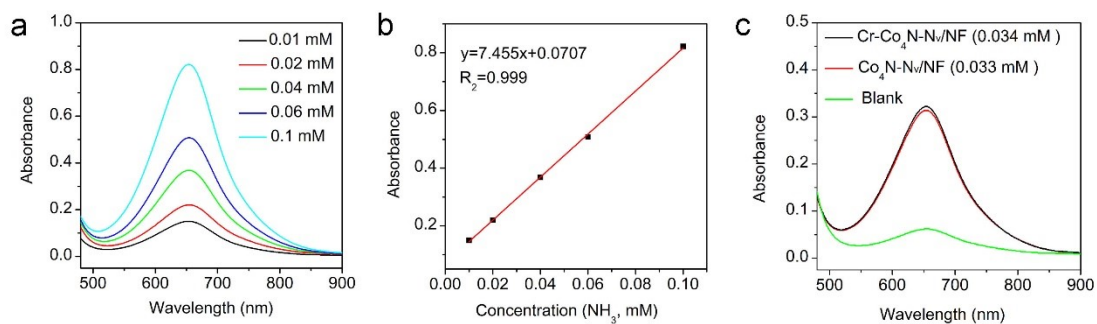
Fig. S7 (a) UV-Vis absorption spectra and (b) the corresponding calibration curve of standard ammonia solutions using the indophenol blue method. (c) The NH_3 concentration in tail gas collected from H_2 treatment of Co_4N/NF (red line) and Cr-Co_4N/NF (black line) by using diluted H_2SO_4 (the size of catalyst is 2 cm * 3 cm).
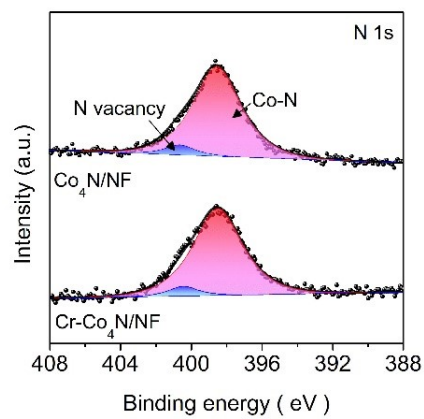
Fig. S8 N 1s XPS spectra of Co$_4$N/NF and Cr-Co$_4$N/NF.
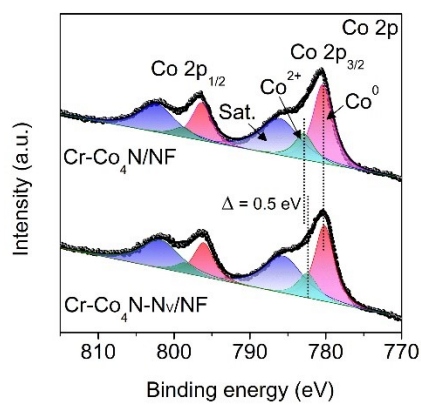
Fig. S9 Co 2p XPS spectra of Cr-Co$_4$N/NF and Cr-Co$_4$N-N$_v$/NF.
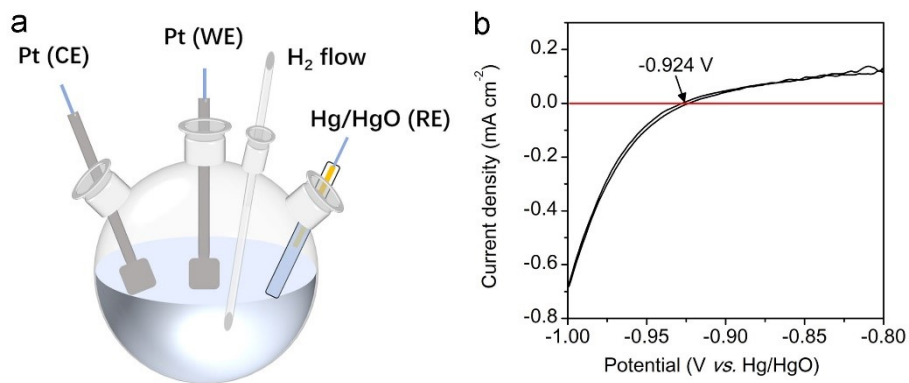
Fig. S10 (a) Experimental setup of the three-electrode cell for reference electrode (RE, Hg/HgO) calibration. Pt foils were used as both working electrode (WE) and counter electrode (CE), and the electrolyte (1 M KOH) was saturated by high-purity H_2. (b) linear sweep voltammetry (LSV) curve of Hg/HgO electrode calibration in 1 M KOH recorded at a scan rate of 1 mV s^{-1} at room temperature. The average of the two interconversion point values was taken as the thermodynamic potential, namely -0.924 V. Therefore, the potential value can be calculated by the following equation: $E_{RHE} = E_{Hg/HgO} + 0.924$.
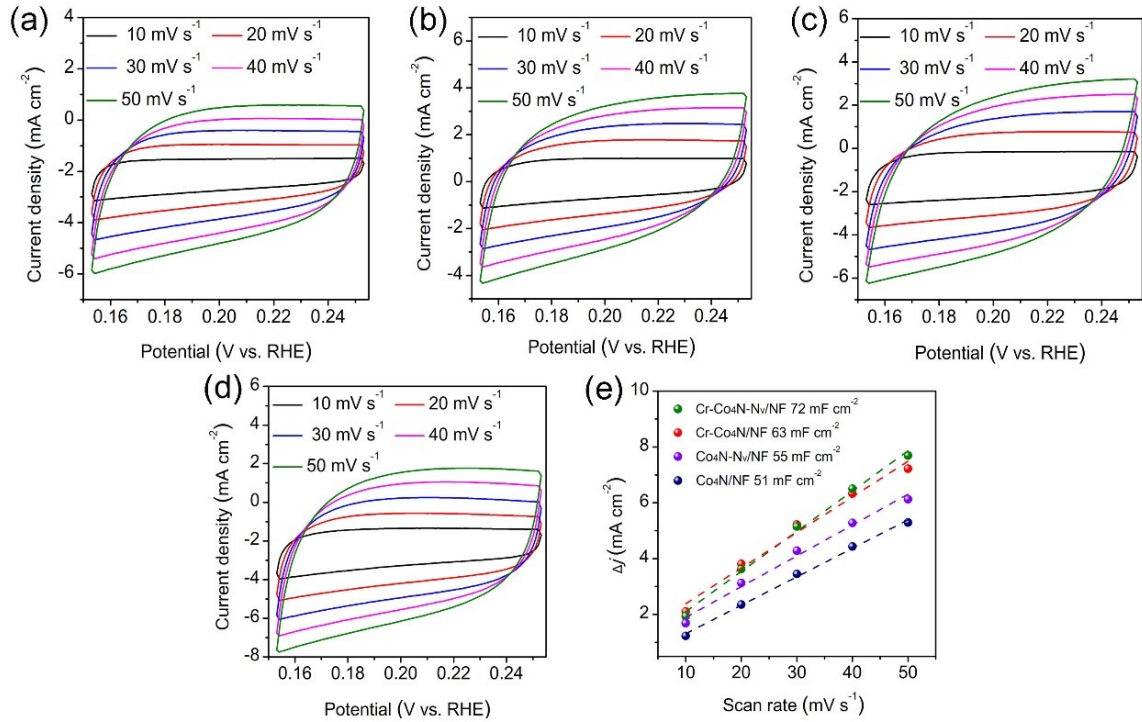
Fig. S11 Cyclic voltammetry curves for (a) Co_4N/NF, (b) Co_4N-N_v/NF, (c) $Cr-Co_4N$ /NF, and (d) $Cr-Co_4N-N_v/NF$ in the non-Faradaic capacitive range at the scanning rate of 10, 20, 30, 40, and 50 mV s^{-1}. (e) The plots of Δj ($\Delta j = j_a - j_c$, j_a and j_c were recorded at 0.20 V vs. RHE) as a function of scan rates for various samples.
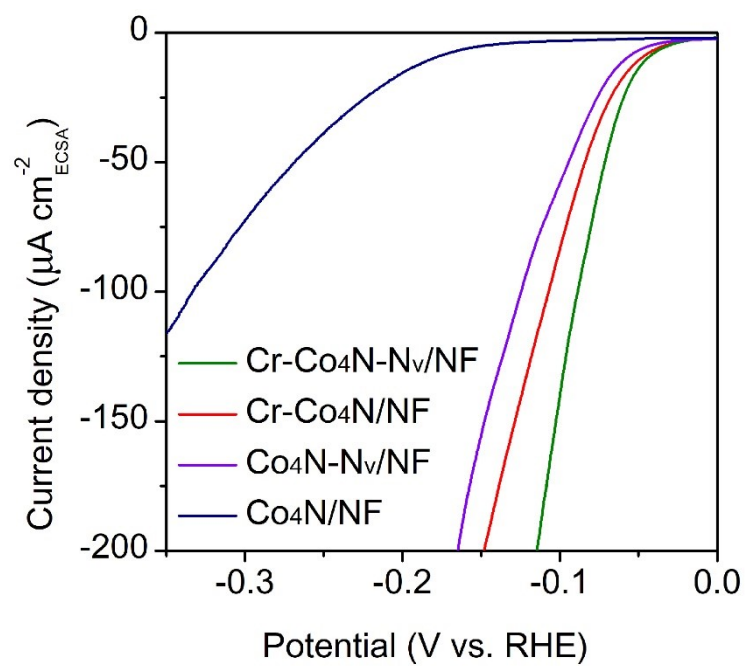
Fig. S12 Specific activities of various catalysts normalized by their corresponding ECSA values.
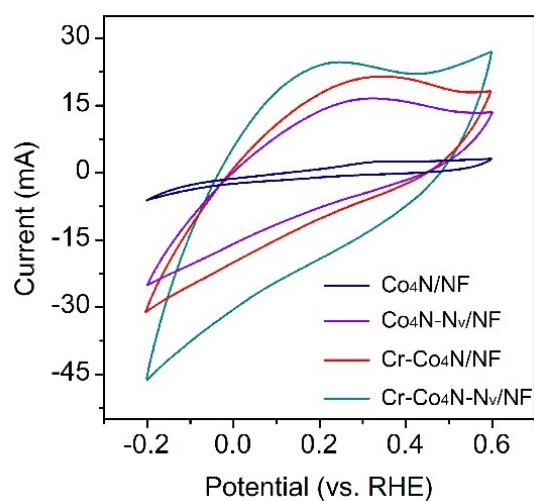
Fig. S13 CV curves over various catalysts measured between -0.2 V and 0.6 V vs. RHE in 1.0 M phosphate buffer saline (PBS) (pH=7) at a scan rate of 50 mV s^{-1}.
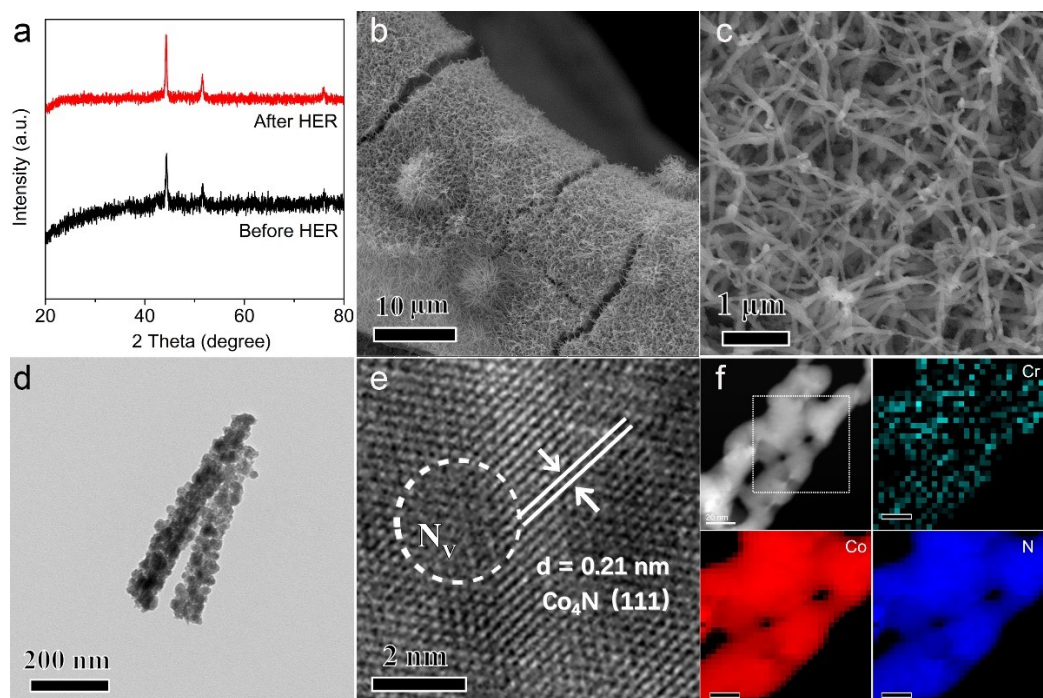
Fig. S14 (a) XRD pattern, (b-c) SEM images, (d) TEM image, (e) HRTEM image, and (f) element mapping of the recovered Cr-Co$_4$N-N$_v$/NF catalyst after 50-h chronopotentiometric test.
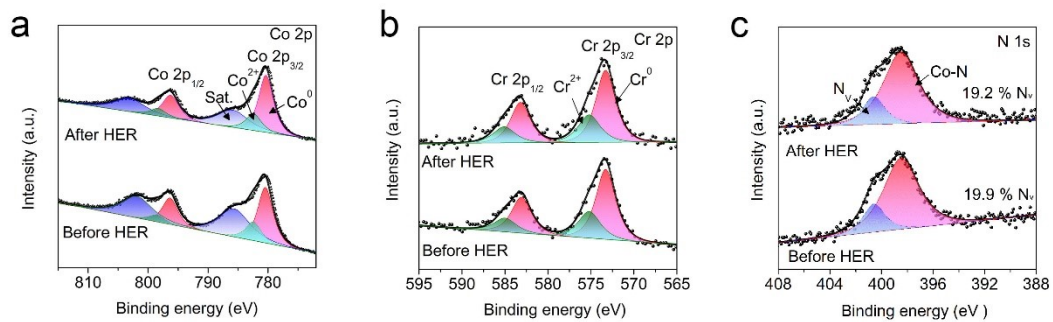
Fig. S15 XPS spectra of (a) Co 2p, (b) Cr 2p, and (c) N 1s of the recovered Cr-Co$_4$N-N$_v$/NF catalyst after 50-h chronopotentiometric test
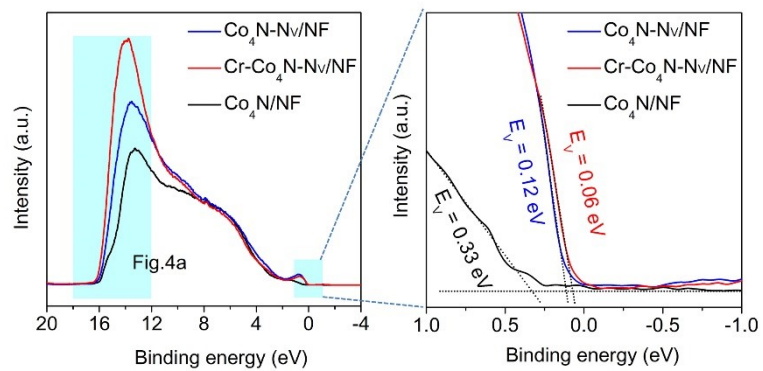
Fig. S16 UPS spectra of Co_4N-N_v/NF, Co_4N/NF, and $Cr-Co_4N-N_v/NF$.
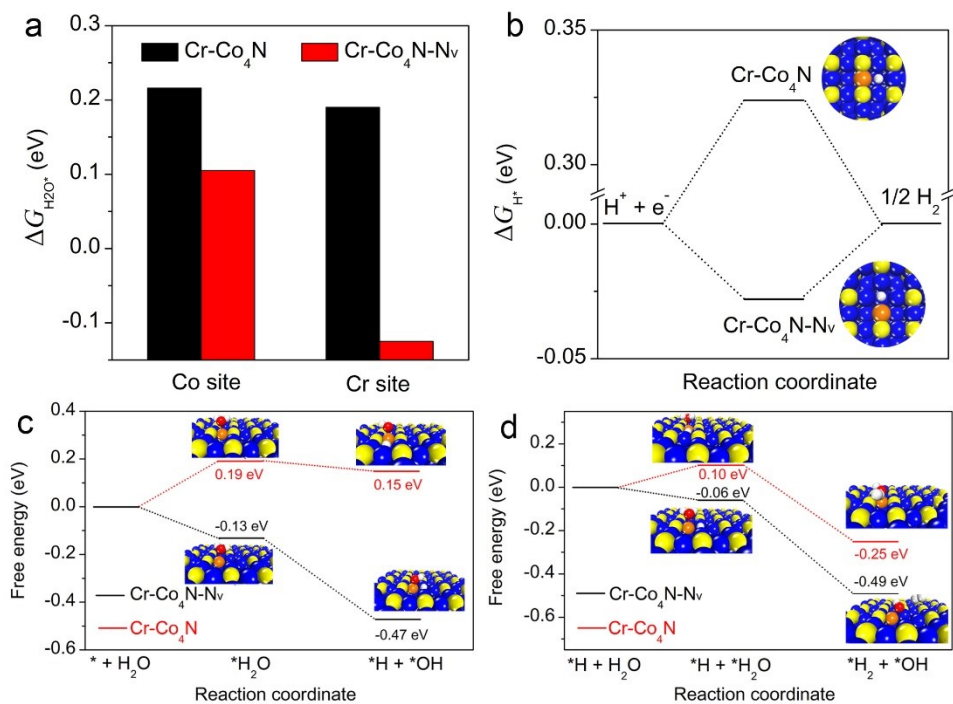
Fig. S17 The calculated free energy for H_2O adsorption (a) and H adsorption (b) over Cr-Co$_4$N-N$_v$ and Cr-Co$_4$N. The energy barrier of water dissociation over Cr-Co$_4$N-N$_v$ and Cr-Co$_4$N via the Volmer (c) and Heyrovsky (d) steps.

21
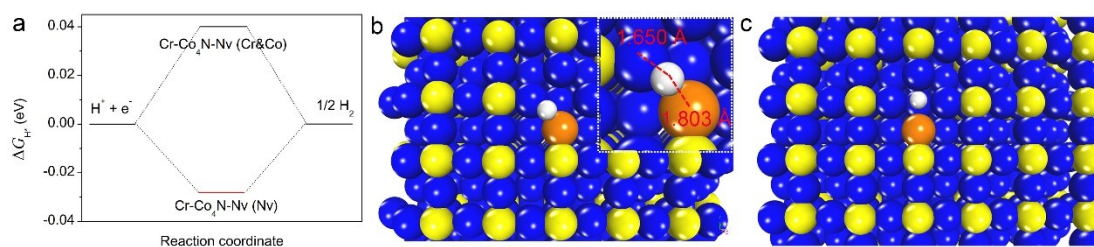
Fig. S18 (a) The Gibbs free energy for H adsorption over different sites of Cr-Co$_4$N-N$_v$ (100), and the corresponding adsorption models: (b) Co and Cr sites on Cr-Co$_4$N-N$_v$ (100) and (c) N$_v$ site on Cr-Co$_4$N-N$_v$ (100). Note that although the Co and Cr sites on the Cr-Co$_4$N-N$_v$ (100) model are initially separately designed for H adsorption, their eventually obtained models are based on the hydrogen bridge between Co and Cr atoms (*i.e.*, Co-H-Cr) and their corresponding ΔG_{H*} are almost identical.
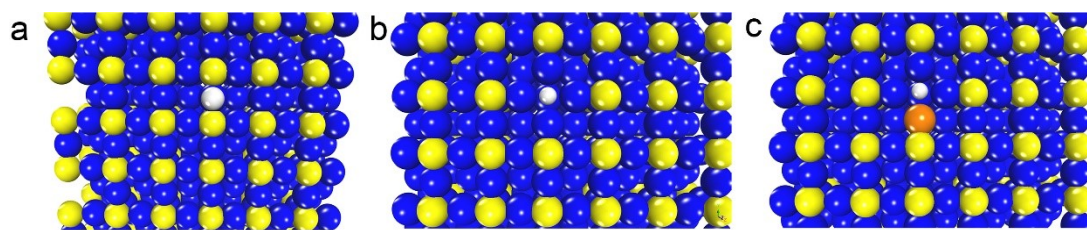
Fig. S19 The simulated models for hydrogen adsorption over various catalysts: (a) Co_4N, (b) Co_4N-N_v, and (c) $Cr-Co_4N-N_v$.
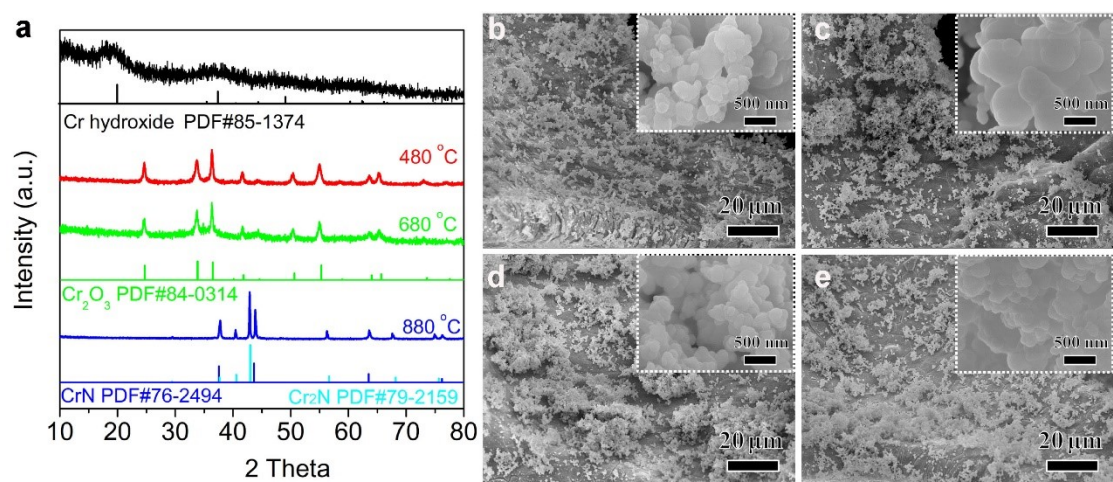
Fig. S20 (a) XRD patterns of various catalysts scarpped from NF substrate. (b-e) SEM images of (b) Cr(OH)F/NF, (c) Cr_2O_3/NF (nitridation at 480 ^{o}C), (d) Cr_2O_3/NF (nitridation at 680 ^{o}C), and (e) CrN-Cr_2N/NF (nitridation at 880 ^{o}C).

Note that Cr_4N was only theoretically constructed,[9, 10] and there was no traceable literature concerning the experimental preparation of Cr_4N. We attempted to synthesize Cr_4N via the nitridation of Cr hydroxide at various temperature ranging from 480 ^{o}C to 880 ^{o}C (Fig. S20). Note that Co_4N and Cr-Co_4N catalysts in our work were prepared in NH_3 atmosphere at 480 ^{o}C. However, when the temperatures for Cr hydroxide nitridation are controlled at 480 and 680 ^{o}C, the obtained samples are oxide rather than nitride (Fig. S20a), which agrees with the results obtained from the previous literature that Cr nitrides, including CrN and Cr_2N, are commonly synthesized at more than 800°C.[11-13] When the calcination temperature increases to 880 ^{o}C, the resulted sample is a mixture of CrN and Cr_2N rather than Cr_4N. Therefore, we think that Cr-Co_4N-N_v indicates Co_4N with Cr-N_v-Co structure rather than a mixture of Co_4N-N_v and Cr_4N-N_v. Moreover, Cr hydroxide, oxide, and nitride grown on NF show the nanoparticle morphology (Fig.S20b-e), while our prepared Cr-Co_4N/NF and Cr-Co_4N-N_v/NF display the nanorod morphology grown on NF. Based on the forementioned discussion, we believe that the Cr nitride species are not formed in Cr-Co_4N-N_v and Cr-Co_4N, and Cr atom exists as a dopant.
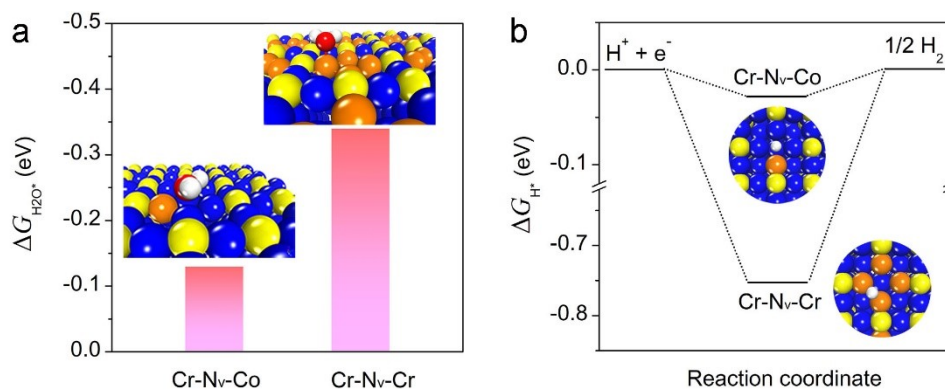
Fig. S21 The calculated free energies for H$_2$O (a) and H (b) adsorption over Cr-N$_v$-Co and Cr-N$_v$-Cr models.

The free energy for H$_2$O adsorption over Cr-N$_v$-Cr model is calculated to be -0.34 eV, lower than that (-0.13 eV) obtained over Co-N$_v$-Cr model (Fig. S21a), indicating that the H$_2$O adsorption process is thermodynamically more favorable over Cr-N$_v$-Cr model. However, the Cr-N$_v$-Cr model suffers from a poor H$_2$ desorption capability relative to the Cr-N$_v$-Co model, as evidenced by its substantially smaller ΔG_{H*} value (-0.753 *vs.* -0.028 eV) (Fig. S21b). Note that the catalyst with ΔG_{H*} close to zero is regarded as the promising candidates for HER.[14] Therefore, the Cr-N$_v$-Co model is believed to show higher HER performance than the Cr-N$_v$-Cr model.

Table S1. The determination of the molar ratio of Cr to Co in different sample using ICP-MS.

Catalysts	Feed molar ratio of Cr to Co	Measured molar ratio of Cr to Co
$Cr-Co_4N/NF$	1 : 20	1 : 19.2
$Cr-Co_4N/NF$	1 : 10	1 : 10.3
$Cr-Co_4N/NF$	1 : 5	1 : 4.8
$Cr-Co_4N-N_V/NF$	1 : 10	1 : 10.5
$Cr-Co_4N-N_V/NF$ after HER	1 : 10	1 : 9.8

Table S2. The HER activity comparison of Co_4N/NF, Co_4N-N_v/NF, $Cr-Co_4N/NF$, $Cr-Co_4N-N_v/NF$ and Pt/C.

	Co_4N/NF	Co_4N-N_v/NF	$Cr-Co_4N/NF$	$Cr-Co_4N-N_v/NF$	Pt/C
η_{10} (mV)	170	51	39	33	33
η_{100} (mV)	307	109	90	73	134

Table S3. The HER activity comparison of the as-prepared $Cr-Co_4N-N_v/NF$ with the emerging metal nitrides reported previously.

Catalysts	η_{10} (mV)	Tafel (mV dec^{-1})	Electrolyte	*Ref.*
$Mo_{0.7}W_{0.3}N_{1.2}$	122	47	1 M KOH	[15]
Co_4N-CeO_2/GP	24	61	1 M KOH	[16]
$Co_3O_4-Mo_2N$	100	162	1 M KOH	[17]
$V-Co_4N/NF$	37	44	1 M KOH	[18]
$Ni-MoN/CF$	24	36	1 M KOH	[19]
Mo_5N_6	94	66	1 M KOH	[20]
$P-MoP/Mo_2N/NF$	89	78	1 M KOH	[21]
Mo_2N-Co_xN/NF	29	53	1 M KOH	[22]
$Co/WN/NF$	27	77	1 M KOH	[23]
$Nb–Ni_3N/NF$	53	112	1 M KOH	[24]
$V–Ni_3N/NF$	83	45	1 M KOH	[25]
$Ni_{0.2}Mo_{0.8}N/Ni_3N/NF$	49	70	1 M KOH	[26]
$Ru-Ni_3N/NF$	32	26	1 M KOH	[27]
$CoMoN_x/NF$	91	70	1 M KOH	[28]
$Se-Co_4N/CFC$	95	55	1 M KOH	[29]
$Cr-Co_4N-N_v/NF$	33	37	1 M KOH	This work

Table S4. The calculated RF values of different samples

Catalysts	Co_4N/NF	$Cr-Co_4N/NF$	Co_4N-N_v/NF	$Cr-Co_4N-N_v/NF$
RF	1275	1587	1375	1800

Table S5. The fitted results of the EIS plots.

Catalysts	Co_4N/NF	$Cr-Co_4N/NF$	Co_4N-N_v/NF	$Cr-Co_4N-N_v/NF$
R_s (Ω)	2.2	2.1	2.2	2.2
R_{CT} (Ω)	19.2	4.8	8.7	3.1

References

1. S. Niu, S. Li, Y. Du, X. Han and P. Xu, *ACS Energy Lett.*, 2020, **5**, 1083-1087.
2. C. C. McCrory, S. Jung, J. C. Peters and T. F. Jaramillo, *J. Am. Chem. Soc.*, 2013, **135**, 16977-16987.
3. J. P. Perdew, K. Burke and M. Ernzerhof, *Phys. Rev. Lett.*, 1996, **77**, 3865.
4. T. Bucko, J. Hafner, S. Lebegue and J. G. Angyan, *J. Phys. Chem. A*, 2010, **114**, 11814-11824.
5. V. Wang, N. Xu, J.-C. Liu, G. Tang and W.-T. Geng, *Comput. Phys. Commun.*, 2021, **267**, 108033.
6. J. K. Nørskov, J. Rossmeisl, A. Logadottir, L. Lindqvist, J. R. Kitchin, T. Bligaard and H. Jonsson, *J. Phys. Chem. B*, 2004, **108**, 17886-17892.
7. M. Dion, H. Rydberg, E. Schröder, D. C. Langreth and B. I. Lundqvist, *Phys. Rev. Lett.*, 2004, **92**, 246401.
8. K. Lee, É. D. Murray, L. Kong, B. I. Lundqvist and D. C. Langreth, *Phys. Rev. B*, 2010, **82**, 081101.
9. M. Meinert, *J. Phys. Condens. Mat.*, 2016, **28**, 056006.
10. A. Azouaoui, N. Benzakour, A. Hourmatallah and K. Bouslykhane, *Solid State Sci.*, 2020, **105**, 106260.
11. Z. Ma, J. Chen, D. Luo, T. Thersleff, R. Dronskowski and A. Slabon, *Nanoscale*, 2020, **12**, 19276-19283.
12. Z. Yang, C. Chen, Y. Zhao, Q. Wang, J. Zhao, G. I. Waterhouse, Y. Qin, L. Shang and T. Zhang, *Adv. Mater.*, 2023, **35**, 2208799.
13. H. Yang, X. Wang, T. Zheng, N. C. Cuello, G. Goenaga, T. A. Zawodzinski, H. Tian, J. T. Wright, R. W. Meulenberg and X. Wang, *CCS Chem.*, 2021, **3**, 208-218.
14. W. Sheng, M. Myint, J. G. Chen and Y. Yan, *Energy Environ. Sci.*, 2013, **6**, 1509-1512.
15. H. Jin, Q. Gu, B. Chen, C. Tang, Y. Zheng, H. Zhang, M. Jaroniec and S.-Z. Qiao, *Chem*, 2020, **6**, 2382-2394.
16. H. Sun, C. Tian, G. Fan, J. Qi, Z. Liu, Z. Yan, F. Cheng, J. Chen, C. P. Li and M. Du, *Adv.*

Funct. Mater., 2020, **30**, 1910596.

17. T. Wang, P. Wang, W. Zang, X. Li, D. Chen, Z. Kou, S. Mu and J. Wang, *Adv. Funct. Mater.*, 2022, **32**, 2107382.

18. Z. Chen, Y. Song, J. Cai, X. Zheng, D. Han, Y. Wu, Y. Zang, S. Niu, Y. Liu and J. Zhu, *Angew. Chem. Int. Ed.*, 2018, **57**, 5076-5080.

19. L. Wu, F. Zhang, S. Song, M. Ning, Q. Zhu, J. Zhou, G. Gao, Z. Chen, Q. Zhou and X. Xing, *Adv. Mater.*, 2022, **34**, 2201774.

20. H. Jin, X. Liu, A. Vasileff, Y. Jiao, Y. Zhao, Y. Zheng and S.-Z. Qiao, *ACS Nano*, 2018, **12**, 12761-12769.

21. Y. Gu, A. Wu, Y. Jiao, H. Zheng, X. Wang, Y. Xie, L. Wang, C. Tian and H. Fu, *Angew. Chem. Int. Ed.*, 2021, **60**, 6673-6681.

22. H. Guo, A. Wu, Y. Xie, H. Yan, D. Wang, L. Wang and C. Tian, *J. Mater. Chem. A*, 2021, **9**, 8620-8629.

23. A. Wu, Y. Gu, B. Yang, H. Wu, H. Yan, Y. Jiao, D. Wang, C. Tian and H. Fu, *J. Mater. Chem. A*, 2020, **8**, 22938-22946.

24. J. Xiang, W. Zou and H. Tang, *Catal. Sci. Technol.*, 2021, **11**, 6455-6461.

25. R.-Q. Li, Q. Liu, Y. Zhou, M. Lu, J. Hou, K. Qu, Y. Zhu and O. Fontaine, *J. Mater. Chem. A*, 2021, **9**, 4159-4166.

26. B. Wang, L. Guo, J. Zhang, Y. Qiao, M. He, Q. Jiang, Y. Zhao, X. Shi and F. Zhang, *Small*, 2022, **18**, 2201927.

27. J. Zhu, R. Lu, W. Shi, L. Gong, D. Chen, P. Wang, L. Chen, J. Wu, S. Mu and Y. Zhao, *Energy Environ. Mater.*, 2023, **6**, e12318.

28. Y. Lu, Z. Li, Y. Xu, L. Tang, S. Xu, D. Li, J. Zhu and D. Jiang, *Chem. Eng. J.*, 2021, **411**, 128433.

29. Y. Sun, K. Mao, Q. Shen, L. Zhao, C. Shi, X. Li, Y. Gao, C. Li, K. Xu and Y. Xie, *Adv. Funct. Mater.*, 2022, **32**, 2109792.